

Article

# Error Analysis and Calibration Improvement of the Imaging Section in a Mueller Matrix Microscope

Jiewei Yu, Xuemin Cheng \*  and Maolin LiShenzhen International Graduate School, Tsinghua University, Shenzhen 518055, China;  
yjw17@mails.tsinghua.edu.cn (J.Y.); limao11108@126.com (M.L.)

\* Correspondence: chengxm@sz.tsinghua.edu.cn

Received: 26 May 2020; Accepted: 23 June 2020; Published: 27 June 2020



**Abstract:** Currently, there are various calibration methods available to reduce the errors caused by the polarizing section of a dual-rotating-retarder polarimeter. Although these methods have high measurement accuracy, their robustness must be improved and the influence of the imaging section needs be discussed when they are applied in Mueller matrix microscopes. In this paper, a method of error source analysis and element calibration for the Mueller matrix microscope is proposed by using error transform coefficient matrices to account for the polarizing effect of the imaging section. Using Taylor expansion, an approximate linear relationship is established between the sources of errors and the Mueller matrix elements of the measured sample. From this relationship, error magnification coefficient matrices are calculated to determine the specific parameter errors in both the polarizing and imaging sections. Furthermore, elements in the fourth row or column of the error magnification coefficient matrix are especially important for the imaging section. The measurement and simulation results for an air sample and a quarter-wave plate sample as the standard samples, as well as a *Daphnia* organism sample with complex internal structure, are investigated and discussed. Furthermore, the comparison results reveal the effect of the imaging section on the birefringence characteristics of the Mueller matrix. With the proposed method, the maximum error can be reduced to be less than 0.01 for all the matrix elements and for the amplitude parameter of birefringence, even when the two system parameters  $a_2$  and  $a_3$  of the rotating mechanical part deviate from the default.

**Keywords:** Mueller matrix; Mueller microscopic imaging; calibration

## 1. Introduction

The technique of polarized light imaging can provide microstructural information on samples, and the Mueller matrix offers a comprehensive description of the polarization properties of samples. Therefore, when the polarized light imaging technique is combined with the Mueller matrix measurement technique, microstructural information can be obtained with great effectiveness [1]. A Mueller matrix microscope is usually designed by adding both the polarization state generator and analyzer (polarizing section) to a microscope (imaging section) and has the ability to measure the Mueller matrix of samples via imaging, which enhances the contrast ratio of the anisotropic structures and has been reported to be extremely helpful in biomedical diagnosis, especially for cancer detection [2,3].

The elements of the Mueller matrix contain all the polarization information necessary for clear and physically meaningful characterization of the measured samples; these elements, either singly or in combination, include diattenuation, retardation, and depolarization. Mueller matrix polar decomposition [4], Mueller matrix transformation [5], and other similar techniques based on transforming polarization parameters are useful and proven tools in biomedicine [6,7], material testing [8], and other fields. Unfortunately, fabrication imperfections and/or assembly misalignment of

the polarizing components in the optical path can lead to errors in the measurement of the Mueller matrix elements. To ensure accurate measurements, the Mueller instrument must be calibrated. One method of doing this is to establish a stabilized optical layout by using a liquid crystal wave plate instead of rotating the mechanical parts for the rotation of the fast axis of the wave plate in the path, thereby improving the stability of the instrument [9]. However, when using a liquid crystal wave plate, the spectral range of the measuring equipment is restricted to the visible spectrum. Under these considerations, the dual-rotating-retarder configuration [10] is applied owing to its relative simplicity. By using a wave plate made of quartz, the spectral range can be expanded from ultraviolet to near-infrared [11]; however, this requires a rotating mechanical part and thereby introduces measurement errors, which presents the need for further calibration.

Several improvements in the mathematical model have been suggested to calibrate the systematic error in a dual-rotating-retarder polarimeter. Hauge treated the characteristics of the wave plate to include diattenuation [12]. Chipman introduced a system model containing not only the retardance error of the wave plates but also the misalignment of the polarizing elements [13]. Li introduced the characteristics of depolarization in the wave plate [14], and Broch et al. discussed the first- and second-order differential forms of the systematic error and presented a scheme of four-zone averaging measurement to obtain stable results [15,16]. Ambirajan and Look [17,18] developed a polarimeter possessing the optimal initial position for a rotating wave plate. Smith [19] further optimized the Mueller matrix polarimeter with respect to the condition number parameter and proved that an overspecified polarimeter with more than 16 states could significantly improve the measurement stability, thus introducing the concept of “instrument matrix” into the polarimeter design. Specifically speaking, there are mainly two different types of methods used to calibrate the systematic error of a Mueller matrix measurement system. The first is the eigenvalue calibration method, which uses a variety of standard Mueller measurement samples to realize complete modeling and calibration of the optical system without calculating the model of each specific device of the polarization state generator and analyzer [20]. The other type of calibration method, in contrast, requires high accuracy of calculation of the misalignments and imperfections of the polarizing elements. The former calibration method results in a better stability without having to change the system structure because of the numerous standard samples, and its convenience and accuracy have been demonstrated for the dual-rotating-retarder configuration [13,21].

As discussed above, errors related to the polarizing section of the Mueller matrix microscope have been addressed by previous conventional calibration methods using the Fourier coefficients of the measured intensities [10]. In our previous study, we also derived a least-square calibration algorithm that shows high accuracy and robustness for the fundamental dual-rotating-retarder Mueller matrix polarimeter [22]. However, because these methods neglect the parasitic polarization induced by imperfections in elements of the imaging section, limitations may exist, and the relative errors could lead to large errors in the calculation of important polarization parameters, such as birefringence. In this study, we propose to completely use the mathematical model for calibration, including both the components in the polarizing and imaging sections, by recasting the Mueller matrices of optical elements in terms of ellipsometric angles. We analyze these systematic errors in a Mueller matrix microscope using the Taylor expansion. Using an optimized combination of controllable error sources, the error magnification coefficient matrices are designed to achieve an approximately linear relationship between the source of the errors and the Mueller matrix element of the measured sample with the precondition of ensuring robustness of the calibration result of the polarizing section. In this way, the specific parameter errors in both the polarizing and imaging sections can be considered, and the robustness is consequently improved.

In Section 2, we discuss the systematic error model using the Taylor expansion of the element in the imaging section. In Section 3, we use calculations and experimental simulation to demonstrate the effect of the proposed calibration method on the calculation of the Mueller matrix of the sample, specifically the birefringence characteristics, by using air, which is isotropic, and quarter-wave plates,

which are anisotropic, as the measurement sample. We also show that these errors can be eliminated or reduced to a proper range, and we perform comparisons of the birefringence of *Daphnia* to demonstrate the general applicability of the proposed method.

## 2. Materials and Methods

### 2.1. Experimental Setup

As shown in Figure 1, we set up a polarized Mueller matrix microscope in our laboratory by integrating a polarization state generator (PSG) and a polarization state analyzer (PSA) into a commercial microscope structure. A light-emitting diode (LED) with a center wavelength of 633 nm and bandwidth of 10 nm was used as the light source. A lens was placed in front of the light source to collimate the diverging light. Both the PSG and PSA contain a fixed linear polarizer (GCL-050003, Daheng Optics, Beijing, China) and a rotating quarter-wave plate (WPQ10ME-633, Thorlabs, Newton, NJ, USA). An electric rotary platform (KPRM1E/M, Thorlabs, Newton, NJ, USA) with angular control precision of 1 arc sec was used to control the angular position of the quarter-wave plate. A 14-bit charge-coupled device (CCD) sensor (Retiga R6, QImaging, Tucson, AZ, USA) was used as the light-intensity detector.

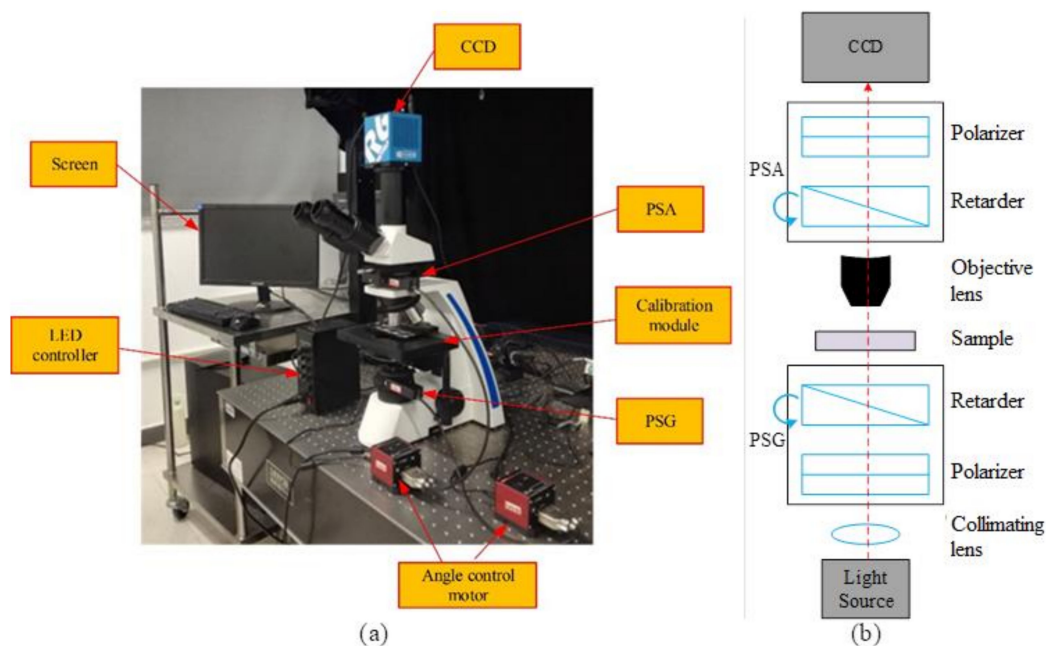


**Figure 1.** (a) Photograph and (b) schematic of the Mueller matrix microscope. Here, CCD: charge-coupled device, LED: light-emitting diode, PSA: polarization state analyzer, and PSG: polarization state generator.

The light emitted by the light source passes through the collimating lens, PSG, measured sample, commercial objective lenses (marked as low polarization or even nonpolarizing [23]), and PSA before being detected by the CCD camera. One common measurement scheme consists of 30 different intensities detected by the CCD; at each step, the wave plate in the PSG is rotated by  $6^\circ$ , and the wave plate in the PSA is rotated by  $30^\circ$  [11]. This measurement scheme has a condition number of the instrument matrix of about 20, which is a minimum value [19], and the measurement scheme was adopted for our instrument. Finally, the Mueller matrix elements were computed from the measured intensities.

### 2.2. Mathematical Model and Calibration Algorithm

As discussed above, system models of a dual-rotating-retarder polarimeter were developed. The Mueller matrix measurement generally involves the establishment and solving of the linear equations described in Equation (1),

$$\vec{P} = W\vec{M} \tag{1}$$

where  $\vec{M}$  is a 16-element column vector composed of all the Mueller matrix elements of the measured sample,  $\vec{P}$  is an  $N$ -element column vector (where  $N$  is 30 times the intensity measurement in the system, as discussed above) composed of the light intensities detected, and  $W$  is an  $N \times 16$  polarimetric measurement matrix. In the conventional calibration method, however, the instrument matrix  $W$  is defined by the parameters of the polarizing elements in the PSG and PSA. Orientation errors of the polarizing elements and retardance errors of the retarders are the primary sources of error, and the evaluation of system parameters  $a_2, a_3, a_4, b_2,$  and  $b_3$  is used to characterize the errors [13]. The system parameters are defined in Figure 2, where  $a_2$  is the angle between the fast axis of the quarter-wave plate and the principal axis of the polarizer in the PSG at the initial time,  $a_3$  is the angle between the fast axis of the quarter-wave plate in the PSA and the principal axis of the polarizer in the PSG at the initial time,  $a_4$  is the angle between the principal axes of the polarizers in the PSG and PSA, and  $b_2$  and  $b_3$  are measures of the actual retardation of the wave plates in the PSG and PSA, respectively; using default values of  $0^\circ, 0^\circ, 0^\circ, 90^\circ,$  and  $90^\circ, a_2, a_3,$  and  $a_4$  were evaluated to indicate the orientation errors of the quarter-wave plate in the PSG, the quarter-wave plate in the PSA, and the polarizer in the PSA, respectively, while  $b_2$  and  $b_3$  were evaluated to indicate the retardance errors of the quarter-wave plates in the PSG and PSA, respectively.

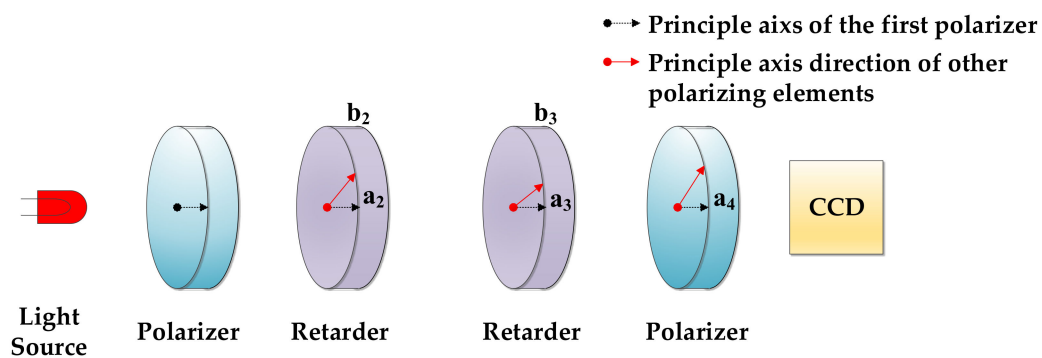


Figure 2. Five system parameters in the polarizing section.

The aforementioned system parameters are used in the polarizing section. In the proposed calibration method, a mathematical model of the imaging section is implemented. To unify the representation of optical elements, we describe the Mueller matrices for each optical element as a function of the system parameters  $\theta, \psi,$  and  $\Delta$ . The partially polarizing effect ( $\psi$ ) and the phase-shifting effect ( $\Delta$ ) are given by Equation (2):

$$M(\theta, \psi, \Delta) = R(-\theta) \begin{bmatrix} 1 & -\cos(2\psi) & 0 & 0 \\ -\cos(2\psi) & 1 & 0 & 0 \\ 0 & 0 & \sin(2\psi) \cos(\Delta) & \sin(2\psi) \sin(\Delta) \\ 0 & 0 & -\sin(2\psi) \sin(\Delta) & \sin(2\psi) \cos(\Delta) \end{bmatrix} R(\theta) \tag{2}$$

where  $\psi$  and  $\Delta$  correspond to the usual ellipsometric angles related to the Fresnel coefficients;  $\theta$  denotes the principle axis orientation angle of different optical elements; and  $R(\theta)$  is the rotation matrix expressed as follows:

$$R(\theta) = \begin{bmatrix} 1 & 0 & 0 & 0 \\ 0 & \cos(2\theta) & -\sin(2\theta) & 0 \\ 0 & \sin(2\theta) & \cos(2\theta) & 0 \\ 0 & 0 & 0 & 1 \end{bmatrix} \tag{3}$$

The system parameters  $\theta$ ,  $\psi$ , and  $\Delta$  in Equation (2) and those in Figure 2 show significant similarities, i.e., the system parameters  $\Delta$ ,  $b_2$ , and  $b_3$  have the polarization meaning of retardance, and  $\theta$ ,  $a_2$ ,  $a_3$ , and  $a_4$  have the physical meaning of angles between the principle axes of different elements. Furthermore, we usually set the principle axis of the first polarizing element to  $0^\circ$ . To model the imaging section in the Mueller matrix microscope, we recast the Mueller matrix of the objective lens using Equations (2) and (3) with the polarization parameters  $\theta_O$ ,  $\psi_O$ , and  $\Delta_O$ . To make the Mueller matrices of the objective lens and air similar, i.e., similar to the identity matrix, the default values of  $\theta_O$ ,  $\psi_O$ , and  $\Delta_O$  are set to  $0$ ,  $\pi/4$ , and  $0$ , respectively. Furthermore, if the values of  $\theta_O$ ,  $\psi_O$ , and  $\Delta_O$  deviate from the default values, the objective lens will cause a change in the polarization characteristics of the incident light. Therefore, the instrument matrix depends not only on the parameters of the polarizing elements but also on those of the objective lens in the imaging section, which can change the polarization state of the incident light.

The conventional calibration method involves derivation of the equations using the Fourier coefficients of the measured intensities, and the calibration performance was reported in Reference [10]. However, the robustness of this method needs to be improved, and the polarization influence, i.e., the birefringence effect of the imaging section must be discussed. In the present study, we re-establish the relationship between the errors caused by the optical elements, including the objective lens, and the Mueller matrix measurement result of the sample. First, it is important to note that random errors of light intensity are also a potential source of measurement error, and as such, Equation (1) should be modified to

$$\vec{P} + \varepsilon\vec{P} = (W + \varepsilon W)(\vec{M} + \varepsilon\vec{M}) \tag{4}$$

where  $\varepsilon\vec{P}$  is the error of the light intensity measured by the CCD,  $\varepsilon\vec{M}$  is the error of the Mueller matrix of the sample, and  $\varepsilon W$  is the error caused by misalignments and imperfections of the polarizing elements and objective lens introduced in the process of constructing the instrument matrix. Then, according to Equations (1) and (4),

$$\varepsilon\vec{M} = \text{pinv}(W + \varepsilon W)\varepsilon\vec{P} - \text{pinv}(W + \varepsilon W)\varepsilon W \cdot \vec{M} \tag{5}$$

where the symbol *pinv* indicates pseudoinverse. In the present dual-rotating-retarder configuration, two fixed linear polarizers are placed in front of the light source and the CCD; therefore, the sensitivity of the CCD and the error caused by the partially polarized source are not considered. Thus, the most crucial factor determining  $\varepsilon\vec{P}$  is the light intensity stability of the light source, and this random error could be reduced by performing repeated measurements. As the light intensity stability of the light source depends on the specific light source used, we will not describe it further in this paper and will reduce Equation (5) to

$$\varepsilon\vec{M} = -\text{pinv}(W + \varepsilon W)\varepsilon W \cdot \vec{M} \tag{6}$$

The instrument matrix used in the experiment is defined by  $W_{\text{exp}} = W + \varepsilon W$ . It depends on the various sources of error:  $W_{\text{exp}}(x_1, x_2, \dots, x_n)$ , where the  $j$ th error source  $x_j$  has the default value  $x_j^{(0)}$ . Then,  $W_{\text{exp}}$  can be expanded in a Taylor series as

$$W_{\text{exp}}(x_1, x_2, \dots, x_n) = W(x_1^{(0)}, x_2^{(0)}, \dots, x_n^{(0)}) + \sum_{j=1}^n \frac{\partial W}{\partial x_j} (x_j - x_j^{(0)}) + \frac{1}{2!} \sum_{j,k=1}^n \frac{\partial^2 W}{\partial x_j \partial x_k} (x_j - x_j^{(0)})(x_k - x_k^{(0)}) + \dots \tag{7}$$

Furthermore, when the higher-order terms in Equation (7) are small, they can be ignored. We first substitute  $W + \varepsilon W$  with  $W_{\text{exp}}$ , where  $\varepsilon W$  is the first-order term in Equation (7) and  $x_j - x_j^{(0)}$  is defined as  $\varepsilon x_j$ . Then, Equation (6) approximately becomes

$$\vec{\varepsilon M} \approx - \sum_{j=1}^n \text{pinv}(W_{\text{exp}}) \frac{\partial W}{\partial x_j} \vec{M} \varepsilon x_j \Big|_{x_j=x_j^{(0)}} \tag{8}$$

The aforementioned expression can be written more succinctly as

$$\begin{aligned} \vec{\varepsilon M} &\approx \sum_{j=1}^n \vec{H}_j \varepsilon x_j \\ \vec{H}_j &= \text{pinv}(W_{\text{exp}}) \frac{\partial W}{\partial x_j} \vec{M} \end{aligned} \tag{9}$$

where the 16-element error-magnifying column vector  $\vec{H}_j$  is introduced to describe the approximately linear mapping between the error sources and the corresponding computed errors of the Mueller matrix. Thus, we can evaluate the errors of the Mueller matrix elements of the sample numerically by using Equation (9).

### 3. Application and Discussion

We applied the proposed calibration method to a standard sample of air (under stable measuring conditions with a temperature of 23.1 °C and humidity of 51%), based on the configuration illustrated in Figure 1, to demonstrate the influence of birefringent parasitic polarization on the Mueller matrix elements of the objective lens in the imaging section and to validate the adaptability of the proposed calibration procedure when using the improved error-propagation model. To examine the general performance, we visually examined and quantified the measurement results of the elements  $M_{24}$ ,  $M_{34}$ ,  $M_{42}$ , and  $M_{43}$ , together with the polarization parameter  $t3$  derived from these elements, as expressed in Equation (10) [24] (which characterizes the amplitude value of birefringence), for an air sample and a quarter-wave plate sample as the standard samples and a Daphnia organism sample with complex internal structure.

$$t3 = \frac{\sqrt{(M_{42})^2 + (M_{34})^2}}{2} = \frac{\sqrt{(M_{43})^2 + (M_{24})^2}}{2} \tag{10}$$

#### 3.1. Calibration Application on a Standard Sample of Air

As mentioned in the introduction section, for the polarizing section, it is sufficient to use the conventional calibration method based on the discrete Fourier coefficients [13,15,16] illustrated in Appendix A. However, in the case of important polarization parameters such as birefringence, the imaging section should be considered for accurate measurement results. We performed computer simulations and experimental measurements on a standard sample of air to reveal the cause of the errors arising from the polarizing section and the imaging section and their propagating effects on the Mueller matrix measurement results. The robustness of the proposed calibration methods was

investigated in comparison to the conventional calibration method. It can be seen from Equation (9) that, assuming an optimized combination of controllable small errors when measuring under stable system conditions, the errors of the measurement results caused by different error sources are independent of each other, i.e.,  $\varepsilon x_j$  is independent of  $\varepsilon x_i (j \neq i)$ ; therefore, we can separately calibrate the polarizing section and imaging section.

When calibrated using the conventional calibration method, the maximum error for the absolute values of the Mueller matrix elements of the measurement configuration without an objective lens could be reduced to 0.01. With the same predefined values of the PSG and PSA ( $a_2, a_3, a_4, b_2,$  and  $b_3$  set to  $0^\circ, 0^\circ, 0^\circ, 90^\circ,$  and  $90^\circ,$  respectively), we first analyzed the parasitic polarization effects in the objective lenses of the imaging section using the conventional method. The Mueller matrix of the objective lens is discussed as follows. This matrix was set to  $M_{obj}(0, \pi/4, 0)$ , identical to the Mueller matrix of air, and this indicated that there were no effects caused by the objective lens. In this case, we obtained the error magnification coefficient matrices of the five system parameters  $a_2, a_3, a_4, b_2,$  and  $b_3,$  as expressed in Equation (11):

$$\begin{aligned}
 H_{a_2} &= \begin{bmatrix} 0 & 0 & 0 & 0 \\ 0 & 0 & -4 & 0 \\ -2 & 4 & 0 & 0 \\ 0 & 0 & 0 & 0 \end{bmatrix}, H_{a_3} = \begin{bmatrix} 0 & 0 & -2 & 0 \\ 0 & 0 & 4 & 0 \\ 0 & -4 & 0 & 0 \\ 0 & 0 & 0 & 0 \end{bmatrix} \\
 H_{a_4} &= \begin{bmatrix} 0 & 0 & 2 & 0 \\ 0 & 0 & -2 & 0 \\ 0 & 2 & 0 & 0 \\ 0 & 0 & 0 & 0 \end{bmatrix}, H_{b_2} = \begin{bmatrix} 0 & 0 & 0 & 0 \\ -1 & 1 & 0 & 0 \\ 0 & 0 & 1 & 0 \\ 0 & 0 & 0 & 0 \end{bmatrix}, H_{b_3} = \begin{bmatrix} 0 & -1 & 0 & 0 \\ 0 & 1 & 0 & 0 \\ 0 & 0 & 1 & 0 \\ 0 & 0 & 0 & 0 \end{bmatrix}.
 \end{aligned} \tag{11}$$

Equation (11) can be used with Equation (9) to obtain the errors in the Mueller matrix for air, which are caused by the polarizing elements. For example, the orientation error of the quarter-wave plate in the PSG ( $a_2$ ) influences the Mueller matrix elements  $M_{23}, M_{31},$  and  $M_{32}$ , and the orientation error of the quarter-wave plate in the PSA ( $a_3$ ) influences the Mueller matrix elements  $M_{13}, M_{23},$  and  $M_{32}$ . However, it also follows from Equation (11) that the error magnification coefficients that may influence the Mueller matrix elements  $M_{11}, M_{14}, M_{24}, M_{34}, M_{41}, M_{42}, M_{43},$  and  $M_{44}$  are zero, implying that the current system parameters in the polarizing section have no effect on these matrix elements.

Generally, the Mueller matrix should be analyzed in normalized form, and the influence on the matrix element  $M_{11}$  is therefore ignored. The error sources for the other matrix elements need to be investigated. For the conventional calibration method, as described in Table A1, the Fourier coefficients  $\alpha_3, \alpha_4, \alpha_6, \alpha_7, \alpha_9, \alpha_{11}, \beta_1, \beta_3, \beta_5, \beta_7, \beta_9,$  and  $\beta_{11}$  are combinations of one or more terms from the fourth row or column of the Mueller matrix. However, the system parameters in the polarizing section are calculated in terms of  $\alpha_2, \alpha_6, \alpha_8, \alpha_{10}, \beta_2, \beta_6, \beta_8,$  and  $\beta_{10}$ , while the system parameter  $a_3$  is calculated in terms of  $\alpha_6$ . Therefore, the fourth row and column of the Mueller matrix have been regarded as redundant and ignored. This, however, results in information loss and calibration inaccuracy. From Equation (11), it can be observed that the matrix elements in the fourth row and fourth column of the error magnification coefficient matrices of the polarizing section are all zeros. To discuss whether these results were the outcome of some particular default values, we also assigned values other than the default values to the system parameters in the polarizing section. The results show that the calculated error magnification coefficients are stable, and the elements in the fourth row and column are always near zero when the five system parameters simultaneously deviate from the default; this indicates that the errors of the measurement system that propagate to these elements cannot be calibrated using the conventional method. One simulation result for the error transform coefficient matrix is shown in Figure 3, where the horizontal axis of each subfigure corresponds to the five parameters in the polarizing section, the vertical axis corresponds to the simulation times, and different colors correspond to the values of the matrix elements. As the maximum absolute value of any element of the error transform coefficient matrices in Equation (11) is 4, random values in the range of  $-0.05$  to  $0.05$  were

assigned to every system parameter (this range was used because it results in a maximum absolute error of 0.2 before the calibration and is available for the visualization of the results, according to the calculated values determined using Equation (9)). Thus, the error magnification coefficient matrix of the imaging section is supplemented, thereby reflecting the error induced by the objective lens, and the calculated results are presented by Equation (12):

$$H_{\theta_O} = \begin{bmatrix} 0 & 0 & 0 & 0 \\ 0 & 0 & 0 & 0 \\ 0 & 0 & 0 & 0 \\ 0 & 0 & 0 & 0 \end{bmatrix}, H_{\psi_O} = \begin{bmatrix} 0 & 2 & 0 & 0 \\ 2 & 0 & 0 & 0 \\ 0 & 0 & 0 & 0 \\ 0 & 0 & 0 & 0 \end{bmatrix}, H_{\Delta_O} = \begin{bmatrix} 0 & 0 & 0 & 0 \\ 0 & 0 & 0 & 0 \\ 0 & 0 & 0 & 1 \\ 0 & 0 & -1 & 0 \end{bmatrix}. \quad (12)$$

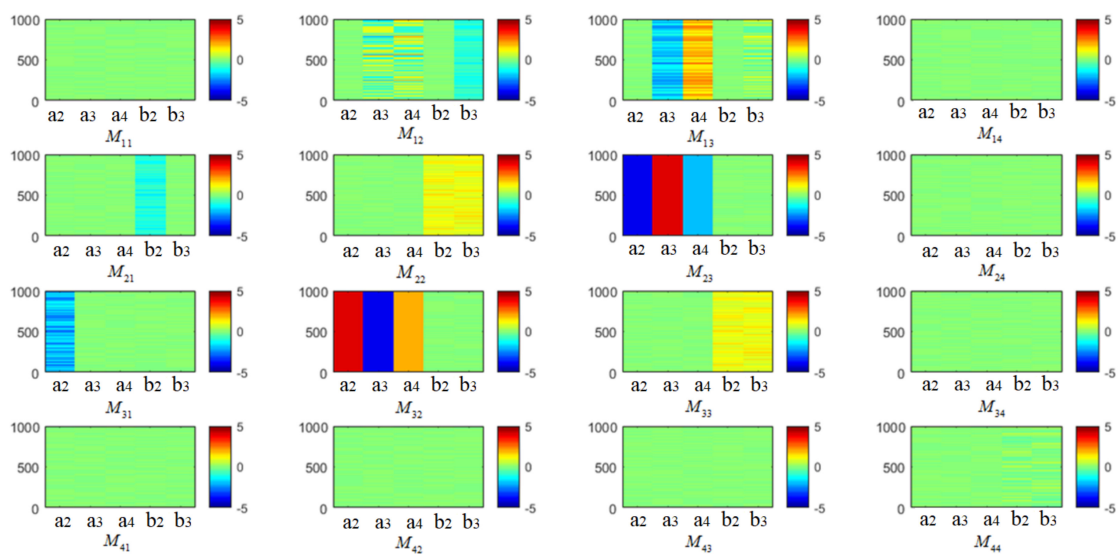


**Figure 3.** Simulation results of the error transform coefficient matrix of the polarizing section of the microscope using the conventional calibration method. In each subfigure, the horizontal axis shows the five polarizing section system parameters, and the vertical axis shows the time. The range of colors indicates the numerical values of the matrix elements. All the values of the fourth row or column are approximately zero, and the element errors caused by the polarizing section are less than 0.01 on these elements for the air sample.

The calculated results for rotation angle  $\theta_O$  and ellipsometric angles  $\psi_O$  and  $\Delta_O$  are shown in Equation (12). Because all the elements in  $H_{\theta_O}$  are zero, Equation (12) indicates that the rotation angle  $\theta_O$  has no effect at any point in time. To test whether the zero results were caused by particular default values, deviating values were once again assigned to the parameters, and the Mueller matrix of the objective lens was reset to  $M_{obj}(0.01, \pi/4 + 0.01, 0.01)$ , although 0.01 is the recommended value according to our experimental results. The error magnification coefficients of the polarizing section were recalculated to ensure accurate calibration. The results, as presented in Table 1(a), Table 1(b), and Figure 4a, show that the maximum error could usually be reduced to 0.01 or less. Elements  $M_{24}$ ,  $M_{34}$ ,  $M_{42}$ , and  $M_{43}$ , even after the polarizing section was calibrated, constitute an exception; therefore, these elements must have been mainly influenced by the imaging section, instead of the polarizing one.

**Table 1.** Average values for the measured Mueller matrix of air (a) before calibration, (b) after calibrating the polarizing section, and (c) after calibrating both the polarizing and imaging sections.

(a)			
1	−0.0724	0.0191	−0.0027
−0.1078	1.1662	−0.1303	−0.0497
−0.0251	1.1151	1.1505	0.0820
0.0054	0.0554	−0.0785	0.9956
(b)			
1	−0.0036	−0.0027	0.0005
−0.0030	1.0095	0.0060	−0.0534
−0.0024	0.0048	0.9969	0.0730
0.0007	0.0476	−0.0725	1.0001
(c)			
1	−0.0036	0.0053	−0.0002
−0.0039	1.0013	−0.0098	0.0070
0.0030	−0.0001	0.9996	0.0087
−0.0008	−0.0025	−0.0084	1.0033

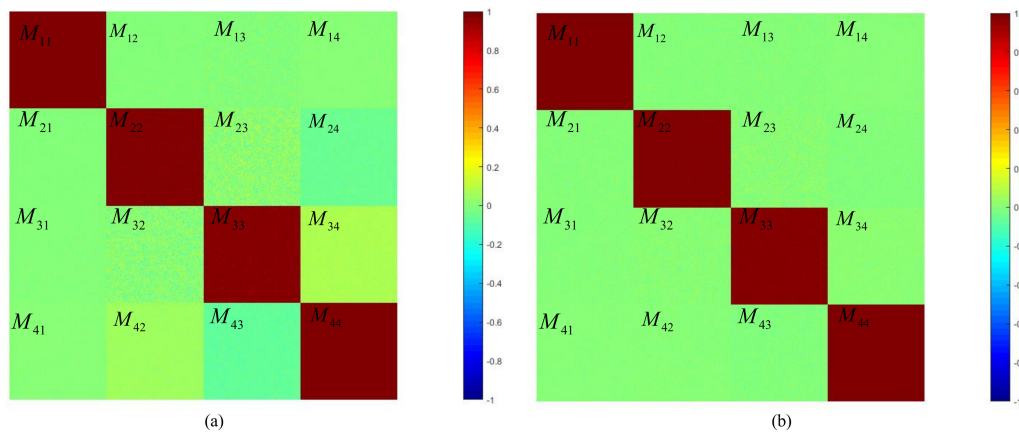


**Figure 4.** Measured Mueller matrix elements of air, presented on a colormap, (a) after calibrating the polarizing section and (b) after calibrating both the polarizing and imaging sections. The  $M_{24}$ ,  $M_{34}$ ,  $M_{42}$ , and  $M_{43}$  elements are closer to zero in (b) as compared to (a), indicating that the imaging section mainly influences the calibration results of these four elements.

Next, the proposed calibration method was applied. Considering the imaging section as well as the polarizing section, the Mueller matrix of air was recalculated; the results are presented in Table 1(c) and Figure 4b, which show that the maximum errors were reduced to less than 0.01 for all the elements. The calibrated system parameters were  $a_2 = -0.0093$ ,  $a_3 = 0.0290$ ,  $a_4 = 0.0263$ ,  $b_2 = 0.0992$ ,  $b_3 = 0.0631$ ,  $\theta_O = 0.2769$ ,  $\psi_O = 0.7844$ , and  $\Delta_O = -0.0905$ .

To test the robustness of the proposed method, the system parameters  $a_2$  and  $a_3$  were also set to several different values around their default values. These two system parameters were singled out because they can be precisely controlled and constrained in a particular range to avoid a large condition number of the instrument matrix. Thus, the values of the system parameters  $a_2$  and  $a_3$  were set to  $-15^\circ$ ,  $-10^\circ$ ,  $-5^\circ$ ,  $0^\circ$ ,  $5^\circ$ ,  $10^\circ$ , and  $15^\circ$ .

Figures 5 and 6 show the calibration results for the air sample when  $a_2$  and  $a_3$  deviate from their default values; Figures 5a and 6a correspond to  $a_2$ , while Figures 5b and 6b correspond to  $a_3$ . The vertical axis shows the difference between the calibration and assumed values. The experimental results clearly show that the calibration result of  $b_3$  determined using the conventional calibration method is unstable (Figure 5b), but the calibration result with the proposed method (Figure 6b) fluctuates only slightly, and the standard deviations of  $b_3$  for the conventional and proposed methods are 1.6772 and

0.0971, respectively. In addition, the calibration results for all the other parameters in the polarizing section have good consistency, indicating that the proposed method is highly robust.

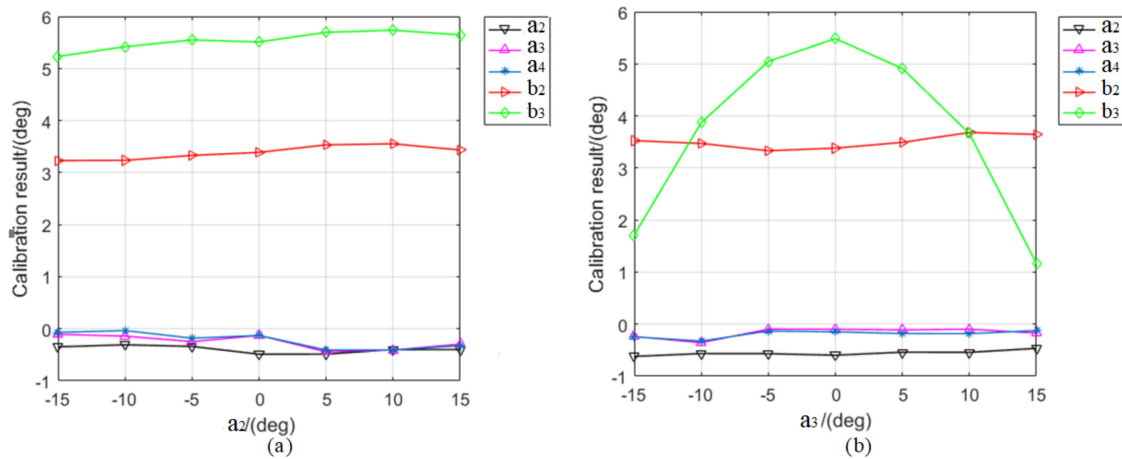


**Figure 5.** Calibration results of the polarizing section using the conventional method when (a)  $a_2$  or (b)  $a_3$  deviates from the default value.

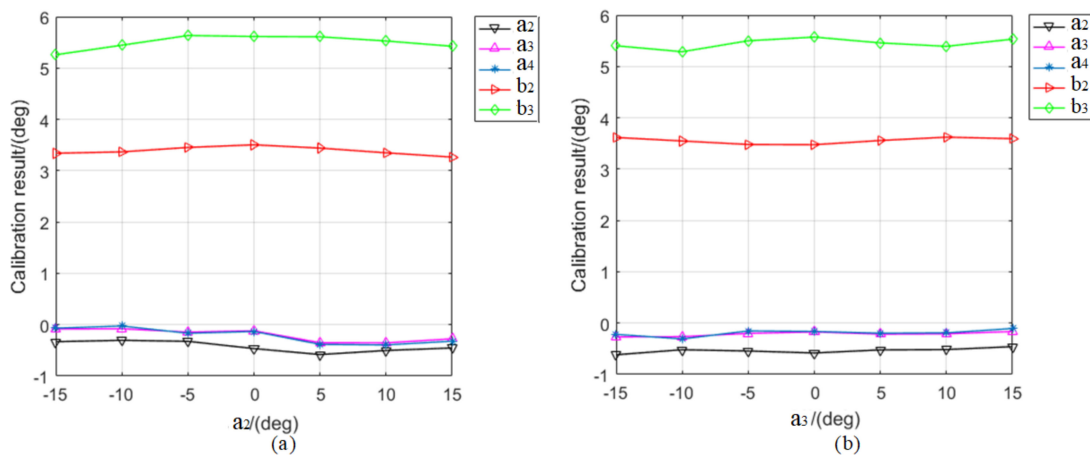


**Figure 6.** Calibration results of the polarizing section using the proposed method when (a)  $a_2$  or (b)  $a_3$  deviates from the default value.

### 3.2. General Applicability

Measured samples often have highly variable content and quality in consideration of the polarization properties. To examine the general applicability of the proposed calibration method, the measurement results of samples of air were first examined; then, a quarter-wave plate with a distinct birefringence effect was selected; and finally, Daphnia, a kind of plankton that demonstrates hierarchical structure details in its dying process, was investigated. The polarization parameter  $t_3$ , which characterizes the amplitude value of birefringence and is derived from elements  $M_{24}$ ,  $M_{34}$ ,  $M_{42}$ , and  $M_{43}$ , was considered to discuss the calibration results of the measurement. In addition, the values of the system parameters  $a_2$  and  $a_3$  were set to  $-15^\circ$ ,  $-10^\circ$ ,  $-5^\circ$ ,  $0^\circ$ ,  $5^\circ$ ,  $10^\circ$ , and  $15^\circ$  in the measurement of the air and the quarter-wave plate samples, while  $a_2$  and  $a_3$  were both set to  $0^\circ$  for the daphnia sample to identify the improvement on its hierarchical structure details.

For the air sample, the measurement results of  $t_3$  (with a theoretical value of 0) shown in Figure 7a are stable when  $a_2$  or  $a_3$  deviates from the default and when the average values are 0.0461 and 0.0455, respectively, meaning that  $t_3$  is independent of  $a_2$  and  $a_3$  and that the errors caused by the imaging section are constant. Thus, after calibrating the imaging section, the order of magnitude of the error of  $t_3$  is reduced to 0.001, as depicted in Figure 7b. Figure 7 depicts not only the difference in the

measurement results of  $t_3$  for the conventional and proposed calibration methods but also the stability of the errors caused by the imaging section. In addition, the measurement results for the quarter-wave plate sample (Figure 8b) are closer to the theoretical value of  $t_3$  (with an average error less than 0.001) and have a stable trend, indicating more stable and accurate test results than those illustrated in Figure 8a.

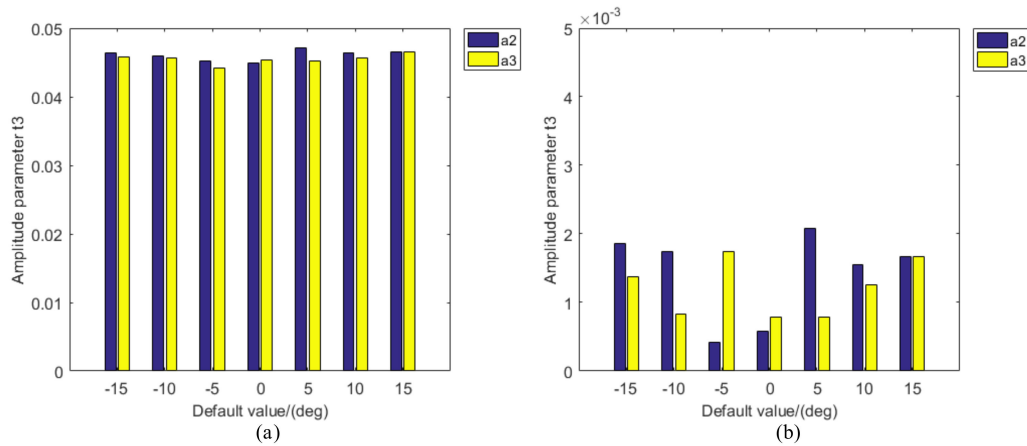


**Figure 7.** Measurement results of  $t_3$  for the air sample (a) after calibrating the polarizing section with the conventional method and (b) after calibrating both the polarizing and imaging sections with the proposed method.

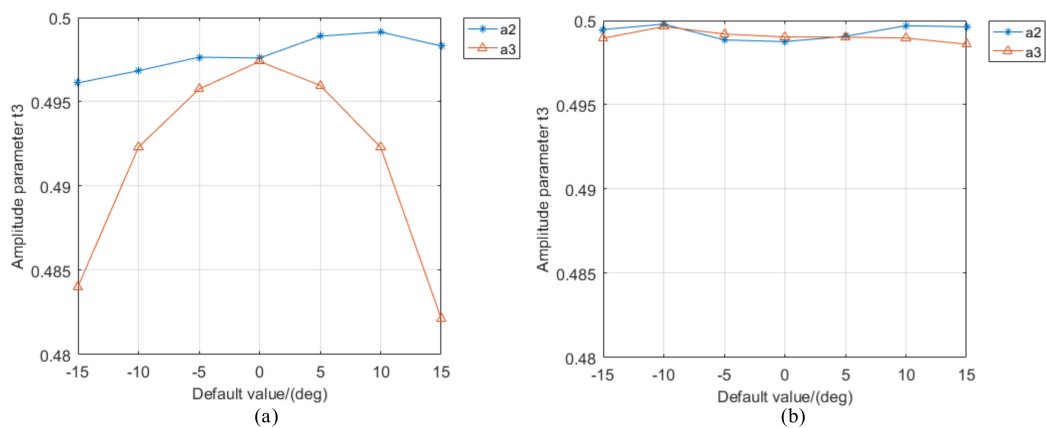


**Figure 8.** Measurement results of  $t_3$  for the quarter-wave plate sample (a) after calibrating the polarizing section with the conventional method and (b) after calibrating both the polarizing and imaging sections with the proposed method.

The calibration result of parameter  $b_3$  in the polarizing section fluctuates considerably (shown in Figure 5b), while the results in Figure 7a are constantly stable, which suggests that the birefringence of air is mainly influenced by the imaging section. For a measurement sample that itself exhibits birefringence, such as the quarter-wave plate (with a theoretical value of 0.5 for  $t_3$ ), the measurement tendencies of  $t_3$  as shown in Figure 8a,b are similar to those of  $b_3$  in Figures 5 and 6, respectively. In other words, the calibration results of parameter  $b_3$  affect the calculation of the birefringence parameter,  $t_3$ , of materials with strong birefringence.

Finally, we compared the calculation accuracy and the clarity of the hierarchical details of the conventional method and the proposed method when imaging plankton samples for the  $t_3$  parameter. A micrograph of the Daphnia sample is shown in Figure 9, and the measurement results of this sample are shown in Figure 10.

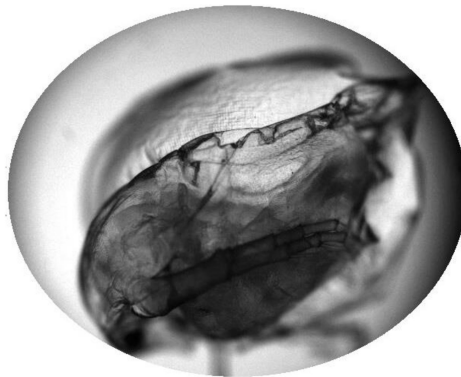


Figure 9. Micrograph of the Daphnia sample.

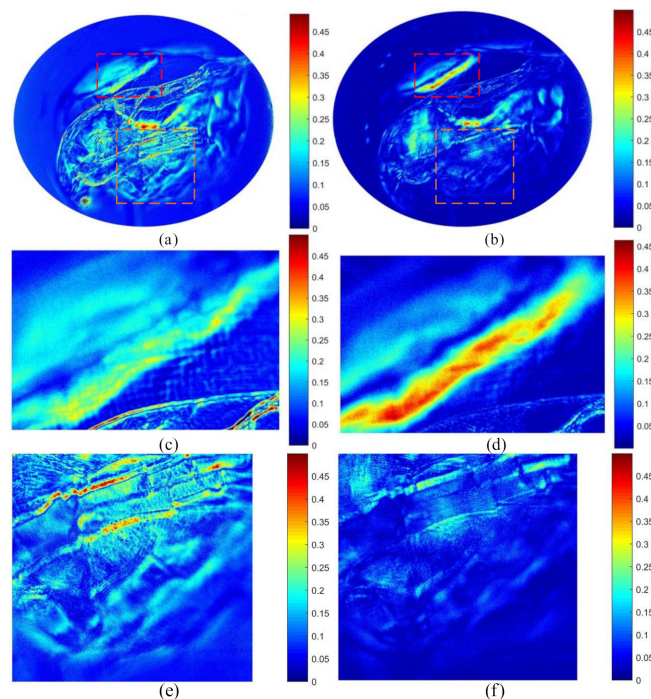


Figure 10. Measurement results of  $t_3$  for the Daphnia sample: (a,c,e) after calibrating the polarizing section with the conventional method; (b,d,f) after calibrating both the polarizing and imaging sections with the proposed method. (c,e) correspond to enlarged views of the red and orange dotted boxes in (a), respectively; (d,f) correspond to enlarged views of the red and orange dotted boxes in (b), respectively.

The Daphnia occupies the middle area, so the pixels at the edge correspond to the air. The  $t_3$  values of the pixels at the edge in Figure 10a are larger than those in Figure 10b; on the other hand, the pixels corresponding to the Daphnia also have large errors, and the birefringence features at these pixels are smaller than the errors caused by the imaging section, thereby leading to an erroneous judgment of the birefringence of the sample. For instance, the values in the red dotted box approximately range from 0.15 to 0.23 in Figure 10c and from 0.29 to 0.47 in Figure 10d, and the values of the orange dotted box area approximately range from 0.15 to 0.36 in Figure 10e but from 0.03 to 0.21 in Figure 10f. The comparison results shown in Figure 10 are similar to those obtained for the air and quarter-wave plates, i.e., when the birefringence of the sample is weak, the calculated value of  $t_3$  is larger than its theoretical value, but  $t_3$  is smaller than its theoretical value for the sample with strong birefringence. Then, the polarization features of Daphnia were recovered, as shown in Figure 10b; this is unlike the results presented in Figure 10a, where the experimental results were severely distorted by the birefringence of the imaging section. Thus, the proposed method possesses considerable advantages in terms of

improving the estimation accuracy of the birefringence caused by the internal structures of the Daphnia and retaining more details of the hierarchical structure of the tissue.

#### 4. Conclusions

We reviewed the configuration for the Mueller microscope (including the imaging section), modeled it mathematically, and presented an intuitive and quantitative scheme for error analysis and calibration. Using the Taylor expansion together with an optimized combination of controllable error sources, we established a relationship between the source of the errors and the calculated Mueller matrix elements. The resulting error magnification coefficient matrices can not only be used to investigate the influence of individual elements in the Mueller matrix but are also helpful for calibrating the imaging section in the Mueller matrix microscope. A comparison of the experimental results confirms that the imaging section introduces measurement error in the Mueller matrix elements, specifically in the fourth row and column. The parasitic polarization of the objective lens can be characterized by the polarization parameter, which describes the birefringence. The maximum error can be reduced to 0.01 after calibrating both the polarizing and imaging sections. Thus, the proposed method is expected to be more advantageous than the conventional methods when using the Mueller microscope in the fields of biomedicine, material testing, and other applications that require accurate knowledge of the elements of the fourth row or column of the Mueller matrix. This method should also be helpful for calibrating particular error sources with large error magnification coefficients. This method is limited by the assumption that the systematic errors are small and that the calculation results for different error sources are mutually independent.

**Author Contributions:** Conceptualization, X.C. and M.L.; Data curation, J.Y.; Funding acquisition, X.C.; Methodology, J.Y. and M.L.; Project administration, X.C.; Software, J.Y.; Supervision, X.C.; Writing—original draft, J.Y.; Writing—review and editing, X.C. All authors have read and agree to the published version of the manuscript.

**Funding:** This research was supported by grants from the National Natural Science Foundation of China (No. 61527826, No. 51735002), the Shenzhen Science and Technology Innovation Program (No. JCYJ20170412171011187), and the National Key Research and Development Program of China (No. 2017YFC1403602).

**Conflicts of Interest:** The authors declare no conflict of interest.

#### Appendix A

For the conventional method [10], the Fourier coefficients of the light intensities contain all the polarization information of the measurement sample, and the relationship between the Fourier coefficients and the Mueller matrix elements of the sample is presented in Table A1.

**Table A1.** Correspondence between the elements of the Mueller matrix and discrete Fourier coefficients of index  $n$ .

$n$	$\alpha_n$	$\beta_n$
0	$\frac{1}{4}M_{11} + \frac{1}{8}M_{12} + \frac{1}{8}M_{21} + \frac{1}{16}M_{22}$	
1	0	$\frac{1}{4}M_{14} + \frac{1}{8}M_{24}$
2	$\frac{1}{8}M_{12} + \frac{1}{16}M_{22}$	$\frac{1}{8}M_{13} + \frac{1}{16}M_{23}$
3	$-\frac{1}{16}M_{43}$	$-\frac{1}{16}M_{42}$
4	$-\frac{1}{8}M_{44}$	0
5	0	$-\frac{1}{4}M_{41} - \frac{1}{8}M_{42}$
6	$\frac{1}{8}M_{44}$	0
7	$\frac{1}{16}M_{43}$	$-\frac{1}{16}M_{42}$
8	$\frac{1}{32}M_{22} + \frac{1}{32}M_{33}$	$-\frac{1}{32}M_{23} - \frac{1}{32}M_{32}$
9	$\frac{1}{16}M_{34}$	$-\frac{1}{16}M_{24}$
10	$\frac{1}{8}M_{21} + \frac{1}{16}M_{22}$	$\frac{1}{8}M_{31} + \frac{1}{16}M_{32}$
11	$-\frac{1}{16}M_{34}$	$\frac{1}{16}M_{24}$
12	$\frac{1}{32}M_{22} - \frac{1}{32}M_{33}$	$\frac{1}{32}M_{23} + \frac{1}{32}M_{32}$

Table A1 presents the discrete Fourier coefficients in terms of Mueller matrix elements. Equation (A1) below expresses the five system parameters of the polarizing section in terms of the discrete Fourier coefficients.

$$\begin{aligned}
 a_2 &= \frac{1}{4} \arctan\left(\frac{\alpha_8}{\alpha_8}\right) - \frac{1}{4} \arctan\left(\frac{\beta_{10}}{\beta_{10}}\right), \\
 a_3 &= \frac{1}{2} \arctan\left(\frac{\beta_2}{\alpha_2}\right) - \frac{1}{2} \arctan\left(\frac{\beta_6}{\alpha_6}\right) + \frac{1}{4} \arctan\left(\frac{\beta_8}{\alpha_8}\right) - \frac{1}{4} \arctan\left(\frac{\beta_{10}}{\alpha_{10}}\right), \\
 a_4 &= \frac{1}{2} \arctan\left(\frac{\beta_2}{\alpha_2}\right) + \frac{1}{2} \arctan\left(\frac{\beta_8}{\alpha_8}\right) - \frac{1}{2} \arctan\left(\frac{\beta_{10}}{\alpha_{10}}\right), \\
 b_2 &= \arccos\left[\frac{\alpha_{10} \cos(4a_3 - 4a_2 - 2a_4) - \alpha_8 \cos(4a_3 - 2a_4)}{\alpha_{10} \cos(4a_3 - 4a_2 - 2a_4) + \alpha_8 \cos(4a_3 - 2a_4)}\right], \\
 b_3 &= \arccos\left[\frac{\alpha_2 \cos(4a_3 - 4a_2 - 2a_4) - \alpha_8 \cos(4a_2 - 2a_4)}{\alpha_2 \cos(4a_3 - 4a_2 - 2a_4) + \alpha_8 \cos(4a_2 - 2a_4)}\right].
 \end{aligned} \tag{A1}$$

## References

1. Wang, Y.; He, H.; Chang, J.; Zeng, N.; Liu, S.; Li, M.; Ma, H. Differentiating characteristic microstructural features of cancerous tissues using Mueller matrix microscope. *Micron* **2015**, *79*, 8–15. [CrossRef]
2. Pierangelo, A.; Nazac, A.; Benali, A.; Validire, P.; Cohen, H.; Novikova, T.; Ibrahim, B.H.; Manhas, S.; Fallet, C.; Antonelli, M.R.; et al. Polarimetric imaging of uterine cervix: A case study. *Opt. Express* **2013**, *21*, 14120–14130. [CrossRef] [PubMed]
3. Jagtap, J.; Chandel, S.; Das, N.; Soni, J.; Chatterjee, S.; Pradhan, A.; Ghosh, N. Quantitative Mueller matrix fluorescence spectroscopy for precancer detection. *Opt. Lett.* **2014**, *39*, 243–246. [CrossRef]
4. Lu, S.Y.; Chipman, R.A. Interpretation of Mueller Matrices Based on Polar Decomposition. *J. Opt. Soc. Am. A* **1996**, *13*, 1106–1113. [CrossRef]
5. He, H.; Zeng, N.; Du, E.; Guo, Y.; Li, D.; Liao, R.; Ma, H. A Possible Quantitative Mueller Matrix Transformation Technique for Anisotropic Scattering Media/Eine Mögliche Quantitative Müller-Matrix-Transformations-Technik Für Anisotrope Streuende Medien. *Photonics Lasers Med.* **2013**, *2*. [CrossRef]
6. Borovkova, M.; Peyvasteh, M.; Dubolazov, O.; Ushenko, Y.; Ushenko, V.; Bykov, A.; Deby, S.; Rehbinder, J.; Novikova, T.; Meglinski, I. Complementary Analysis of Mueller-Matrix Images of Optically Anisotropic Highly Scattering Biological Tissues. *J. Eur. Opt. Soc. Rapid Publ.* **2018**, *14*. [CrossRef]
7. Liu, B.; Yao, Y.; Liu, R.Q.; Ma, H.; Ma, L. Mueller Polarimetric Imaging for Characterizing the Collagen Microstructures of Breast Cancer Tissues in Different Genotypes. *Opt. Commun.* **2019**, *433*, 60–67. [CrossRef]
8. Song, B.K.; Gu, H.G.; Zhu, S.M.; Jiang, H.; Chen, X.G.; Zhang, C.W.; Liu, S.Y. Broadband Optical Properties of Graphene and HOPG Investigated by Spectroscopic Mueller Matrix Ellipsometry. *Appl. Surf. Sci.* **2018**, *439*, 1079–1087. [CrossRef]
9. Aas, L.M.S.; Ellingsen, P.G.; Fladmark, B.E.; Letnes, P.A.; Kildemo, M. Overdetermined Broadband Spectroscopic Mueller Matrix Polarimeter Designed by Genetic Algorithms. *Opt. Express* **2013**, *21*, 8753–8762. [CrossRef]
10. Li, J.A.; Ramanujam, B.; Collins, R.W. Dual Rotating Compensator Ellipsometry: Theory and Simulations. *Thin Solid Films* **2011**, *519*, 2725–2729. [CrossRef]
11. Azzam, R.M.A. Photopolarimetric Measurement of Mueller Matrix by Fourier-Analysis of a Single Detected Signal. *Opt. Lett.* **1978**, *2*, 148–150. [CrossRef] [PubMed]
12. Hauge, P.S. Mueller Matrix Ellipsometry with Imperfect Compensators. *J. Opt. Soc. Am. A* **1978**, *68*, 1519–1528. [CrossRef]
13. Chenault, D.B.; Pezzaniti, J.L.; Chipman, R.A. Mueller Matrix Algorithms. *Proc. SPIE Int. Soc. Opt. Eng.* **1992**, *1746*, 231–246.
14. Li, W.Q.; Zhang, C.W.; Jiang, H.; Chen, X.G.; Liu, S.Y. Depolarization Artifacts in Dual Rotating Compensator Mueller Matrix Ellipsometry. *J. Opt.* **2016**, *18*, 055701. [CrossRef]
15. Broch, L.; Naciri, A.E.; Johann, L. Systematic Errors for a Mueller Matrix Dual Rotating Compensator Ellipsometer. *Opt. Express* **2008**, *16*, 8814–8824. [CrossRef]
16. Broch, L.; Naciri, A.E.; Johann, L. Second-Order Systematic Errors in Mueller Matrix Dual Rotating Compensator Ellipsometry. *Appl. Opt.* **2010**, *49*, 3250–3258. [CrossRef]
17. Ambirajan, A.; Look, D.C. Optimum Angles for a Polarimeter .1. *Opt. Eng.* **1995**, *34*, 1651–1655. [CrossRef]
18. Ambirajan, A.; Look, D.C. Optimum Angles for a Polarimeter .2. *Opt. Eng.* **1995**, *34*, 1656–1658. [CrossRef]

19. Smith, M.H. Optimization of a Dual-Rotating-Retarder Mueller Matrix Polarimeter. *Appl. Opt.* **2002**, *41*, 2488–2493. [[CrossRef](#)]
20. Compain, E.; Poirier, S.; Drevillon, B. General and Self-Consistent Method for the Calibration of Polarization Modulators, Polarimeters, and Mueller-Matrix Ellipsometers. *Appl. Opt.* **1999**, *38*, 3490–3502. [[CrossRef](#)]
21. Li, W.; Zhang, C.; Chen, X.; Gu, H.; Liu, S. Mueller Matrix Polarimeter with Imperfect Compensators: Calibration and Correction. In Proceedings of the Computational Optical Sensing and Imaging, Kohala Coast, HI, USA, 22–26 June 2014; p. CW3C.3. [[CrossRef](#)]
22. Cheng, X.; Li, M.; Zhou, J.; Ma, H.; Hao, Q. Error Analysis of the Calibration of a Dual-Rotating-Retarder Mueller Matrix Polarimeter. *Appl. Opt.* **2017**, *56*, 7067–7074. [[CrossRef](#)] [[PubMed](#)]
23. Daugherty, B.; Chipman, R. Low Polarization Microscope Objectives. In Proceedings of the SPIE 7652, International Optical Design Conference 2010, Jackson Hole, WY, USA, 9 September 2010; Bentley, J., Gupta, A., Eds.; Spie-Int Soc Optical Engineering: Bellingham, WA, USA, 2010; Volume 76521S, pp. 1–8.
24. He, H.; Chang, J.; He, C.; Ma, H. Transformation of full  $4 \times 4$  Mueller matrices: a quantitative technique for biomedical diagnosis. *Proc. SPIE* **2016**, *9707*, 9707K. [[CrossRef](#)]



© 2020 by the authors. Licensee MDPI, Basel, Switzerland. This article is an open access article distributed under the terms and conditions of the Creative Commons Attribution (CC BY) license (<http://creativecommons.org/licenses/by/4.0/>).